Real-projective-plane hybrid-order topological insulator realized in phononic crystals

Pengtao Lai,[1,‖] Jien Wu,[2,‖] Zhenhang Pu,[3] Qiuyan Zhou,[3] Jiuyang Lu,[3] Hui Liu,[1] Weiyin Deng,[3,*] Hua Cheng,[1,†] Shuqi Chen,[1,4,‡] and Zhengyou Liu[3,5,§]

[1] *The Key Laboratory of Weak Light Nonlinear Photonics, Ministry of Education, Smart Sensing Interdisciplinary Science Center, School of Physics and TEDA Institute of Applied Physics, Nankai University, Tianjin 300071, China*

[2] *School of Physics and Optoelectronics, South China University of Technology, Guangzhou, Guangdong 510640, China*

[3] *Key Laboratory of Artificial Micro- and Nanostructures of Ministry of Education and School of Physics and Technology, Wuhan University, Wuhan 430072, China*

[4] *The Collaborative Innovation Center of Extreme Optics, Shanxi University, Taiyuan, Shanxi 030006, China*

[5] *Institute for Advanced Studies, Wuhan University, Wuhan 430072, China*

(Received 29 November 2023; revised 7 March 2024; accepted 15 March 2024; published 1 April 2024)

The manifold of the fundamental domain of the Brillouin zone is always considered to be a torus. However, under the synthetic gauge field, the Brillouin manifold can be modified by the projective symmetries, resulting in unprecedented topological properties. Here, we realize a real-projective-plane hybrid-order topological insulator in a phononic crystal by introducing the Z_2 gauge field. Such an insulator hosts two momentum-space nonsymmorphic reflection symmetries, which change the Brillouin manifold from a torus to a real projective plane. These symmetries can simultaneously lead to a Klein-bottle insulator and quadrupole insulator phases in different bulk gaps. The nonsymmorphic reflection symmetries on Brillouin real-projective-plane, edge states of the Klein-bottle insulator, and corner states of the quadrupole insulator are observed. These results evidence the hybrid-order topology on the Brillouin manifold beyond the torus, and enrich the topological physics.

DOI: 10.1103/PhysRevApplied.21.044002

I. INTRODUCTION

Symmetry plays a key role in the classification of topological matter [1–3]. In the presence of gauge field, the algebraic structures of crystal symmetries can be projectively enriched and generate the so-called projective symmetries, opening up avenues for topological physics [4,5]. A case in point is that the π gauge flux can change the commute relation for reflection symmetries to the anticommute one, forming the projective reflection symmetries and leading to the multipole insulator [6,7]. Among them, the quadrupole insulator is the two-dimensional second-order topological phase, and featured with the zero-dimensional corner states [8]. Recently, a unified discussion about the projective symmetry algebra based on Z_2 gauge field (0 and π flux over the lattices) in the two dimensions has been constructed [9]. Under a Z_2 gauge field, the projective translation symmetry can give rise to the Möbius topological insulator [10,11], the projective mirror symmetry leads to the mirror Chern insulator [12–14], and the projective PT symmetry can switch the spinless and spinful topological phases [15–18].

Interestingly, the Z_2 gauge field can modify the manifold of the fundamental domain of the Brillouin zone (BZ), giving rise to unprecedented topological phenomena. The Brillouin manifold is usually known as a torus. In the presence of Z_2 gauge field, the real-space reflection symmetry can be projectively represented, which generates the momentum-space nonsymmorphic (MSNS) reflection symmetry that performs glide reflection in momentum space [19]. In two dimensions, a single MSNS refection symmetry can change the Brillouin manifold from a torus to a Klein bottle, and give rise to the Klein-bottle insulator (KBI), which possesses the first-order topology described by Z_2 invariant and hosts a pair of edge states with a nonlocal twist [20]. Abundant topologies on the Brillouin Klein bottle are further discovered [21–26], including the first

*dengwy@whu.edu.cn
†hcheng@nankai.edu.cn
‡schen@nankai.edu.cn
§zyliu@whu.edu.cn
‖These authors contributed equally to this work.

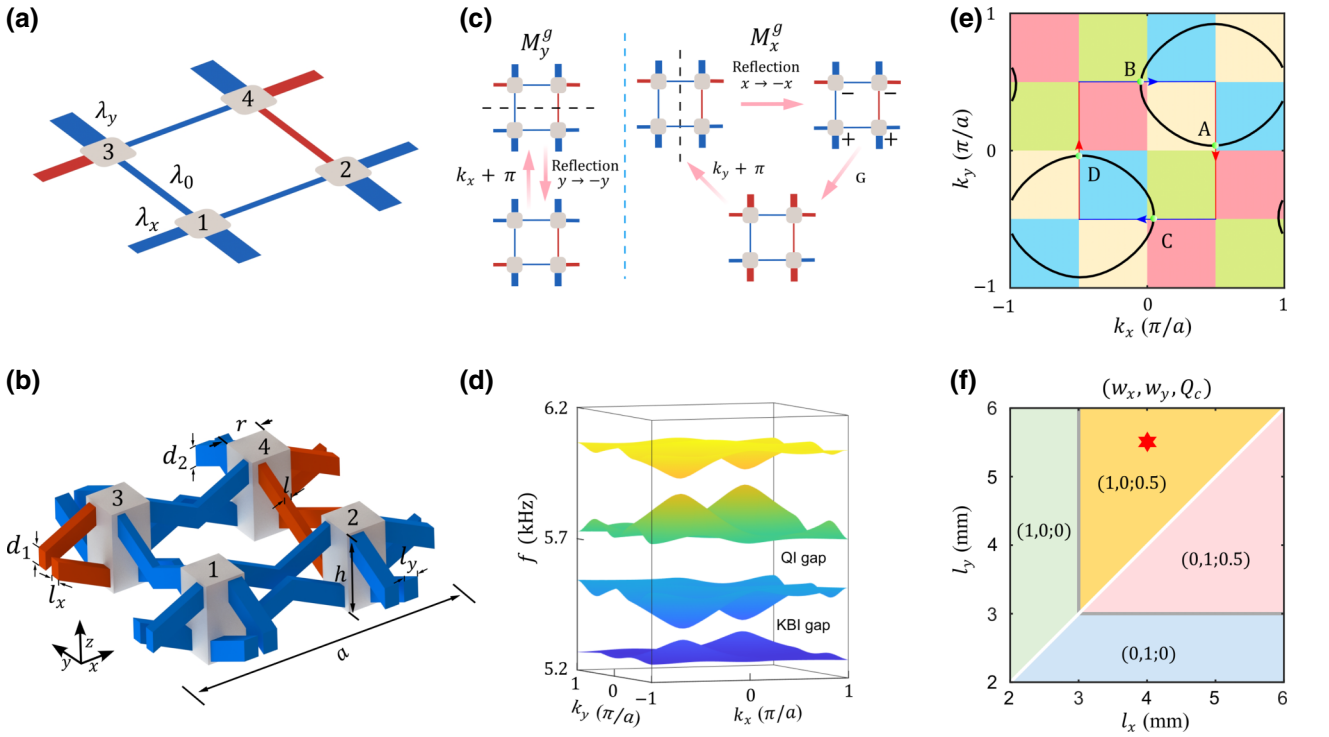

FIG. 1. Acoustic real-projective-plane HOTI protected by the MSNS reflection symmetries M_x^g and M_y^g. (a),(b) Unit cells of tight-binding model and PC. Red (blue) tubes represent negative (positive) couplings. (c) Schematics of MSNS reflection symmetries. (d) Bulk dispersion of PC with KBI and QI gaps. (e) Isofrequency contours (black curves) of PC at 5.5 kHz in the first BZ. The reduced BZ (enclosed by the red and blue arrows) can be regarded as a real projective plane. (f) Phase diagram determined by Z_2 invariants $(w_x,\ w_y)$ of KBI gap and corner charge Q_c of QI gap in the l_x-l_y plane. The white (gray) line denotes the phase boundary of KBI (QI). The red star represents the hybrid-order topological phase with specific parameters used in (b),(d).

order and higher order. Very recently, it has been proposed that a pair of MSNS reflection symmetries can reduce the Brillouin manifold from a torus to a real projective plane, and give rise to the second-order topological phase [27,28]. Experimental exploration of the intriguing topology on the Brillouin real projective plane beyond the traditional paradigm is therefore necessary.

Here, we realize an acoustic real-projective-plane hybrid-order topological insulator (HOTI), which hosts a KBI phase with first-order topology and a quadrupole insulator (QI) phase with second-order topology in two bulk gaps. Due to the macroscopic scale, phononic crystal (PC) for acoustic waves is a versatile platform to explore the abundant topological physics [29–31]. The synthetic Z_2 gauge field can be achieved by accurately designing the positive and negative couplings in the PC [32–35]. We first illustrate the MSNS reflection symmetries and the ensuing Brillouin real projective plane and topological phase diagram in the PC. We then observe the bulk properties on Brillouin real projective plane, KBI edge states, and QI corner states in a practical PC sample. The experimental results, in agreement with the theoretical ones, evidence the hybrid-order topology on Brillouin real projective plane.

II. BRILLOUIN REAL PROJECTIVE PLANE

Corresponding to the unit cell of the lattice model shown in Fig. 1(a), the unit cell of the designed PC contains the same four acoustic resonant cavities with height $h = 30$ mm and width $r = 15$ mm, as illustrated in Fig. 1(b). The resonance frequency of the cavities' P_z mode is $f_0 = c_0/(2h) = 5.68$ kHz, where $c_0 = 341$ m/s is the speed of sound in air. The lattice constant $a = 110.62$ mm. The intracell tubes with size $l = 3$ mm and intercell tubes with sizes $l_x = 4$ mm and $l_y = 5.5$ mm are constructed as the intracell and intercell couplings, which are at a distance of 10 mm to the top or bottom surfaces of cavities. The red and blue tubes act as the negative and positive couplings with $d_1 = 7$ mm and $d_2 = 8$ mm, as discussed in Sec. SI within the Supplemental Material [36]. With the cavities viewed as the lattice sites and the tubes acting as the couplings, the PC can be well mapped by the tight-binding model (see Sec. SI within the Supplemental Material [36]). The Bloch Hamiltonian on the basis of sublattices 1–4 can be written as

$$H(k_x,\ k_y) = \lambda_0(\Gamma_{01} + \Gamma_{13}) + \lambda_x(\cos k_x\Gamma_{31} + \sin k_x\Gamma_{32}) + \lambda_y(\cos k_y\Gamma_{10} + \sin k_y\Gamma_{20}), \quad (1)$$

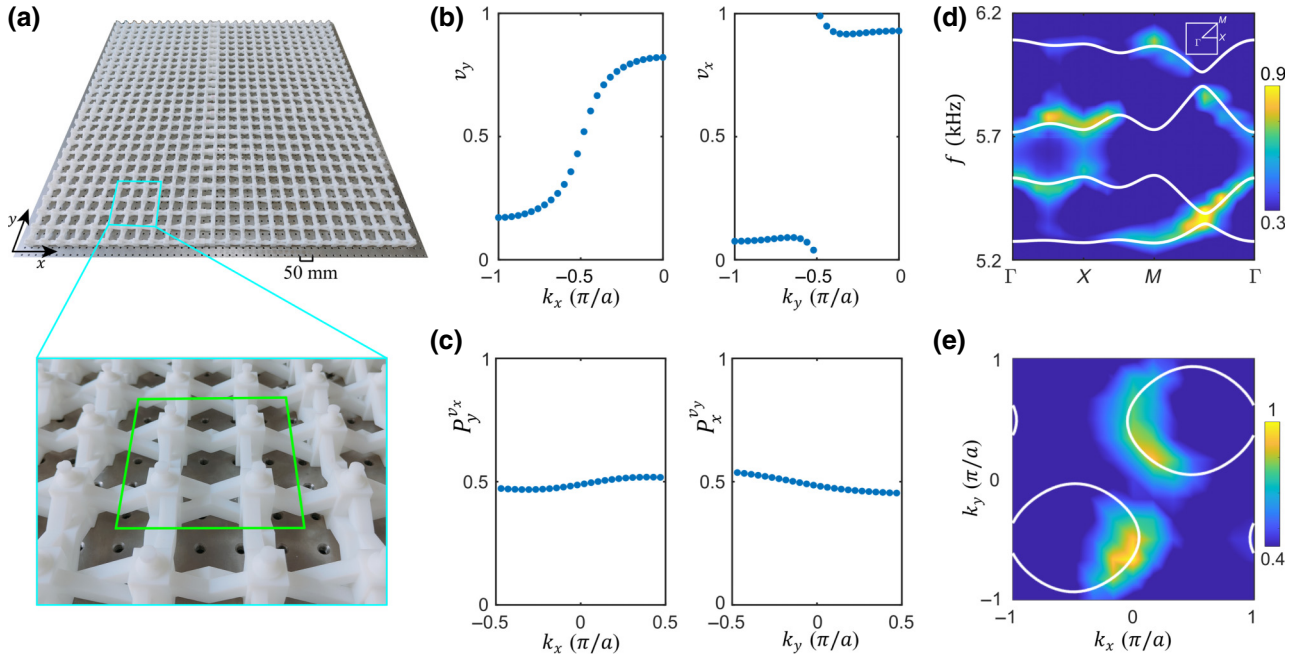

FIG. 2. Observation of bulk properties of acoustic real-projective-plane HOTI. (a) Photograph of PC sample. The enlarged sample shows the detailed configuration of unit cell enclosed by green lines. (b) Calculated Wannier bands v_y and v_x of the first band of PC, which indicates the Z_2 invariants $(w_x,\ w_y) = (1,\ 0)$. (c) Calculated Wannier sector polarizations $P_y^{v_x}$ and $P_x^{v_y}$ of the lowest two bands of PC, revealing the quantized quadrupole moment. (d) Measured (color map) and calculated (white lines) dispersions along the Γ–*X*–*M*–Γ lines. (e) Measured and calculated isofrequency contours at 5.5 kHz.

where $\Gamma_{ij} = \tau_i \otimes \sigma_j$, τ_0 (σ_0) is the 2×2 identity matrix, τ_i and σ_i with $i = 1,\ 2,\ 3$ are Pauli matrices for the degrees of freedom within a unit cell. The lattice constant is set to unity, λ_0 is the intracell coupling, λ_x and λ_y are the intercell couplings along the x and y directions, respectively.

The PC possesses a pair of MSNS reflection symmetries $M_x^g = GM_x = \Gamma_{31}$ and $M_y^g = \Gamma_{10}$, where M_x represents the normal reflection in the x direction and $G = \Gamma_{30}$ is the gauge transformation. M_x^g and M_y^g satisfy the anticommute relation $\{M_x^g, M_y^g\} = 0$. In momentum space, we have

$$M_y^g H(k_x, k_y)(M_y^g)^{-1} = H(k_x + \pi, -k_y), \tag{2}$$

$$M_x^g H(k_x, k_y)(M_x^g)^{-1} = H(-k_x, k_y + \pi). \tag{3}$$

To visualize these two symmetries, we illustrate the processes of the symmetric transformation. As shown in the left panel of Fig. 1(c), for M_y^g symmetry, the unit cell is reflected in the y direction, then recovered by transforming k_x into $k_x + \pi$. For M_x^g symmetry, the unit cell is reflected in the x direction, and needed to apply a gauge transformation G by assigning a sign of $+1$ or -1 to the basis at each site, finally recovered by transforming k_y to $k_y + \pi$, as illustrated in the right panel of Fig. 1(c).

The MSNS reflection symmetries M_x^g and M_y^g reduce the BZ of PC to form a real-projected-plane manifold, which will act on the bulk dispersions shown in Figs. 1(d) and 1(e). The first BZ is divided into 16 regions, and each region with the same color can be linked by the M_x^g, M_y^g or $M_x^g M_y^g$ symmetry, as shown in Fig. 1(e). The central region of the BZ ($[-\pi/2, \pi/2] \times [-\pi/2, \pi/2]$) consists of four regions marked by different colors, which contains the full information of the first BZ. Thus, we can define a reduced BZ of the central region as the fundamental domain of the first BZ. Interestingly, the boundaries of such reduced BZ are oppositely oriented via M_x^g and M_y^g symmetries, as shown by the red and blue arrows in Fig. 1(e), and glued together to form a real-projective-plane manifold [37]. As a concrete example, we extract the isofrequency contours of bulk dispersion at 5.5 kHz, as depicted by the black curves in Fig. 1(e). All contours in the first BZ can be mapped from those in the real-projective-plane BZ. Under the M_y^g (M_x^g) symmetry, A (B) point is transformed into D (C) point on the isofrequency contours.

The MSNS reflection symmetries M_x^g and M_y^g can give rise to hybrid-order topology on the Brillouin real projective plane. As shown in Fig. 1(d), the four bulk bands can have three bulk gaps, in which the lower and upper gaps are the gaps of KBI and the middle gap is the gap of QI. The KBI possesses the first-order topology described by Z_2 invariants w_x and w_y, while the QI is characterized by corner charge Q_c that is defined by the quadrupole moment and edge polarizations, as discussed in detail in Secs. SII and SIII within the Supplemental Material [36].

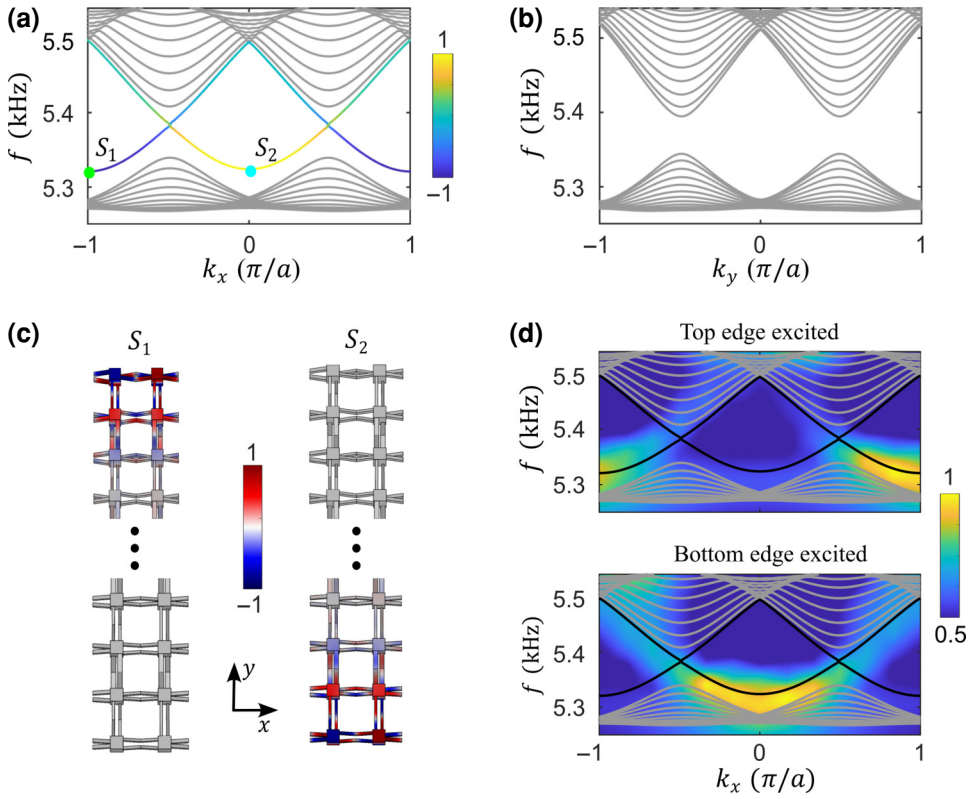

FIG. 3. Observation of edge states in the KBI gap. (a) Calculated projected dispersions along the x direction. The colored lines represent a pair of edge states with a nonlocal twist in the KBI gap, and the color denotes the degree of localization at the top (blue) and bottom (yellow) boundaries. (b) Calculated projected dispersion along the y direction. There is no edge state in the KBI gap. (c) Eigenfield distributions of edge modes at S_1 ($k_x = -\pi/a$) and S_2 ($k_x = 0$) points marked in (a), which are connected by M_y^g symmetry. (d) Measured edge dispersions (color maps) excited at the centers of the top and bottom boundaries, respectively. The black lines are the calculated edge dispersions in (a).

For simplicity, we focus on the topological properties of the lower and middle gaps. Figure 1(f) shows the topological phase diagram determined by $(w_x, w_y; Q_c)$, in which w_x and w_y are calculated in the first band and Q_c is for the lowest two bands. There exist four topological phases in the l_x-l_y plane. Phases with $(1, 0; 0)$ and $(0, 1; 0)$ are the first-order topological phases with zero corner charge, while those with $(1, 0; 0.5)$ and $(0, 1; 0.5)$ are hybrid-order topological phases with nonzero first-order and second-order topological invariants simultaneously. The white line is the phase boundary of KBI with bulk gap closure, and the gray line is that of QI with edge gap closure, as shown in Sec. SIV within the Supplemental Material [36].

We now experimentally reveal the MSNS reflection symmetries and Brillouin real projective plane in the PC. Figure 2(a) shows the PC sample fabricated by three-dimensional (3D) printing technology with $(l_x, l_y) = (4\ \text{mm}, 5.5\ \text{mm})$, corresponding to the parameters labeled as the red star in Fig. 1(f). The positive and negative hopping terms are realized by the coupling waveguides with different configurations. We calculate the Wannier bands $v_y(k_x)$ and $v_x(k_y)$ of the first bulk band by using its eigenfield, as shown in Fig. 2(b). As k_x (k_y) varies from $-\pi/a$ to 0, the Wannier band $v_y(k_x)$ ($v_x(k_y)$) passes through 0.5 with odd (even) times, which indicates the nontrivial (trivial) Z_2 invariant $w_x = 1$ ($w_y = 0$) in the x (y) direction (Sec. SII within the Supplemental Material [36]). We also calculate the Wannier sector polarization $P_y^{v_x}$ and $P_x^{v_y}$ of the lowest two bands, as shown in Fig. 2(c), and obtain nonzero quadrupole moment $q_{xy} = 2P_y^{v_x}P_x^{v_y} = 0.5$. The corner charge Q_c can be calculated as $Q_c = p_x^e + p_y^e - q_{xy}$, where $p_x^e = 0.5$ and $p_y^e = 0.5$ are edge polarizations (Sec. SIII within the Supplemental Material [36]), leading to $Q_c = 0.5$. So this PC is a HOTI with $(w_x, w_y; Q_c) = (1, 0; 0.5)$. Figure 2(d) plots the calculated (white lines) and measured (color map) bulk dispersions along the Γ–M–X line. The calculated and measured isofrequency contours at 5.5 kHz are displayed in Fig. 2(e), denoting the existence of special MSNS reflection symmetry and ensuing real projective plane in momentum space. The measured and calculated isofrequency contours at different frequencies are further shown in Sec. SV within the Supplemental Material [36]. The measured bulk dispersions are obtained by Fourier transforming the

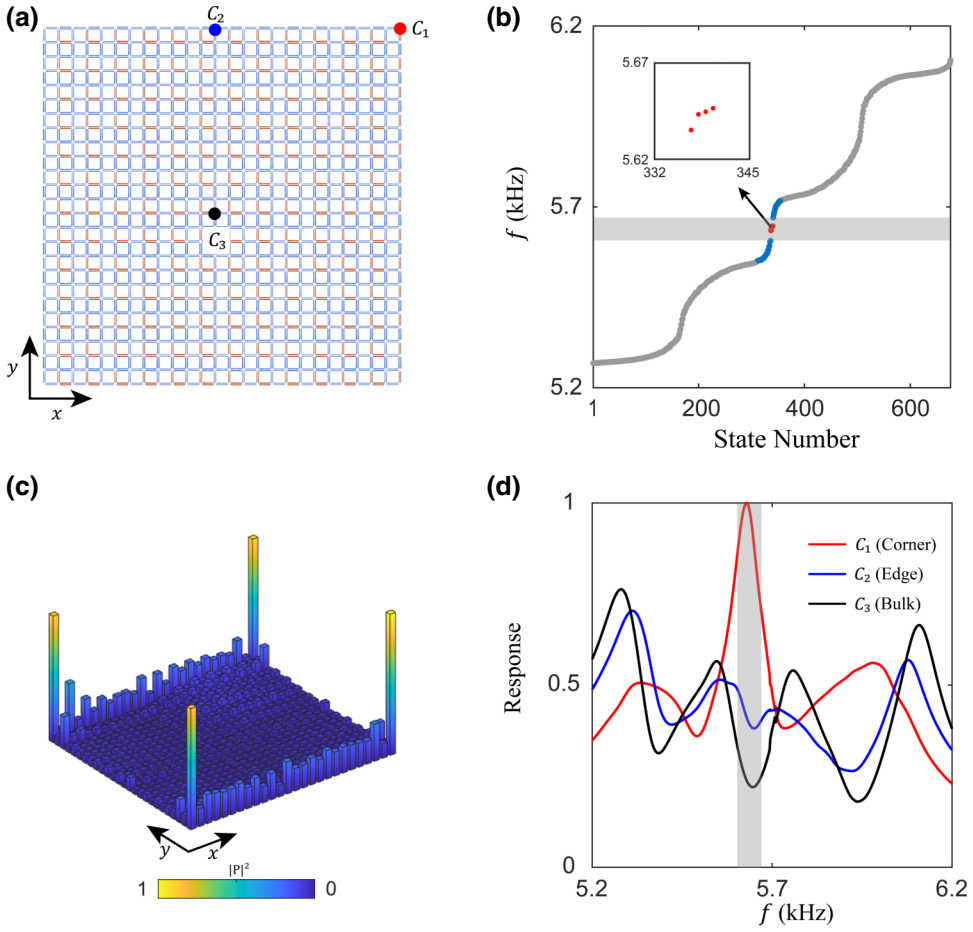

FIG. 4. Observation of corner states in the QI gap. (a) Schematic of square-shaped PC sample. (b) Eigenfrequency spectrum. The blue and red dots denote the edge and corner modes in the QI gap, respectively. Inset: enlarged region for corner states. (c) Measured pressure field distribution at 5.65 kHz, demonstrating the existence of corner states. (d) Measured response spectra at the positions C_1, C_2, and C_3, which are normalized by the maximum value.

measured field, where the source is placed at the center of the PC sample. Therefore, the designed PC is a real-projected-plane HOTI.

III. FIRST-ORDER TOPOLOGY IN THE FIRST BULK GAP

According to the bulk-boundary correspondence, the real-projected-plane HOTI supports a pair of edge states with a nonlocal twist in the KBI gap. A PC ribbon is built to investigate the edge states along x (y) direction, which has a periodic boundary condition in the x (y) direction, and finite-size length in the y (x) direction. Figures 3(a) and 3(b) show the calculated projected dispersions along x and y directions, respectively. It can be seen that the edge bands (colored lines) in the KBI gap emerge only in the x direction, correspondence to the Z_2 invariants $(w_x, w_y) = (1, 0)$. The color denotes the localization of edge state ψ_e at the bottom (yellow) and top (blue) boundaries, which is defined as $d = \sum_{x\in b} |\psi_e(x)|^2 - \sum_{x\in t} |\psi_e(x)|^2$ and b (t) represents the outermost two unit cells of the bottom (top) boundary. Due to the M_y^g symmetry, the eigenfrequency at k_x is the same as that at $k_x + \pi/a$, and their eigenfields are connected by the y directional reflection symmetry, behaving as a nonlocal twist. For example, the frequency at S_1 ($k_x = -\pi/a$) is equal to that at S_2 ($k_x = 0$). The eigenfield distributions of edge modes at S_1 and S_2 are shown in Fig. 3(c), where the color maps represent the acoustic pressures normalized by their maximum value. One can see that the fields of S_1 and S_2 are localized at top and bottom boundaries, respectively, which satisfy $M_y^g \psi_{S_1} = \psi_{S_2}$ and verify the existence of MSNS reflection symmetry.

In experiments, we first place a source at the center of the top boundary and measure the response pressure of cavities in this boundary. After Fourier transforming the measured data, the projected dispersion is obtained and shown in the upper panel of Fig. 3(d). More details about the experiment are shown in Sec. SVI within the Supplemental Material [36]. Notably, only the edge modes near $k_x = \pm\pi/a$ are excited, demonstrating that the fields of

these modes are mainly localized on the top boundary like S_1. The edge modes near $k_x = 0$ are excited by the source at the bottom boundary, revealing the localization of these edge modes on the bottom boundary like S_2, as shown in the lower panel of Fig. 3(d). These results are consistent with the calculated ones in Fig. 3(a), together revealing the edge states with a nonlocal twist.

IV. SECOND-ORDER TOPOLOGY IN THE SECOND BULK GAP

Finally, we demonstrate the existence of corner states in the QI gap of the real-projected-plane HOTI, attributed to $Q_c = 0.5$. The square-shaped PC with 13×13 unit cells is depicted in Fig. 2(a), and its schematic is displayed in Fig. 4(a). Figure 4(b) shows the eigenfrequency spectrum, where the corner states (red dots) emerge in the QI gap. The inset displays four corner modes near the frequency 5.65 kHz. In the experiment, the source excites at each cavity and the response of acoustic pressure is measured at the same cavity. Figure 4(c) shows the measured pressure-field distribution at frequency 5.65 kHz of corner states. One can see that the measured field is localized at four corners of the PC sample. We further measure the broadband response of acoustic pressures at corner (C_1), edge (C_2), and bulk (C_3), as shown in Fig. 4(d), where the data are normalized by the maximum value. The resonant peak of pressure at the corner is observed in the band gap, which is larger than that at the edge and bulk at the same frequency.

V. CONCLUSIONS

In conclusion, we have realized a real-projected-plane HOTI in a PC, where the BZ is reduced by a pair of MSNS reflection symmetries to form a real projective plane. It is noted that real-projected-plane topological insulator in Refs. [27,28] focus only on the second-order topological states in the second band gap. Different from the previous works [26–28,31], the real-projected-plane HOTI simultaneously hosts that a KBI phase features a pair of edge states with a nonlocal twist in the lower gap and a QI phase characterizes nontrivial corner states in the middle gap. Our work represents an experimental extension of band topology on Brillouin manifold from a torus to a real projected plane. With the flexibility in achieving the synthetic gauge field, our system may serve as a basis for further exploration of nontrivial topological properties on three-dimensional Brillouin manifold beyond the real projected plane.

ACKNOWLEDGMENTS

This work is supported by the National Key R&D Program of China (Grants No. 2022YFA1404501, No. 2022YFA1404900, and No. 2021YFA1400601), the National Natural Science Fund for Distinguished Young Scholars (Grant No. 11925403), the National Natural Science Foundation of China (Grants No. 12074128, No. 12122406, No. 12192253, and No. 12374409), and the Guangdong Basic and Applied Basic Research Foundation (Grant No. 2022B1515020102).

[1] A. P. Schnyder, S. Ryu, A. Furusaki, and A. W. W. Ludwig, Classification of topological insulators and superconductors in three spatial dimensions, Phys. Rev. B **78**, 195125 (2008).
[2] C.-K. Chiu, J. C. Y. Teo, A. P. Schnyder, and S. Ryu, Classification of topological quantum matter with symmetries, Rev. Mod. Phys. **88**, 035005 (2016).
[3] B. Bradlyn, L. Elcoro, J. Cano, M. G. Vergniory, Z. Wang, C. Felser, M. I. Aroyo, and B. A. Bernevig, Topological quantum chemistry, Nature **547**, 298 (2017).
[4] Y. X. Zhao, Y.-X. Huang, and S. A. Yang, Z_2-projective translational symmetry protected topological phases, Phys. Rev. B **102**, 161117 (2020).
[5] L. B. Shao, Q. Liu, R. Xiao, S. A. Yang, and Y. X. Zhao, Gauge-field extended $k{\cdot}p$ method and novel topological phases, Phys. Rev. Lett. **127**, 76401 (2021).
[6] W. A. Benalcazar, B. A. Bernevig, and T. L. Hughes, Quantized electric multipole insulators, Science **357**, 61 (2017).
[7] W. A. Benalcazar, B. A. Bernevig, and T. L. Hughes, Electric multipole moments, topological multipole moment pumping, and chiral hinge states in crystalline insulators, Phys. Rev. B **96**, 245115 (2017).
[8] B. Xie, H. X. Wang, X. Zhang, P. Zhan, J. H. Jiang, M. Lu, and Y. Chen, Higher-order band topology, Nat. Rev. Phys. **3**, 520 (2021).
[9] Z. Y. Chen, Z. Zhang, S. A. Yang, and Y. X. Zhao, Classification of time-reversal-invariant crystals with gauge structures, Nat. Commun. **14**, 743 (2023).
[10] H. Xue, Z. Wang, Y. X. Huang, Z. Cheng, L. Yu, Y. X. Foo, Y. X. Zhao, S. A. Yang, and B. Zhang, Projectively enriched symmetry and topology in acoustic crystals, Phys. Rev. Lett. **128**, 116802 (2022).
[11] T. Li, J. Du, Q. Zhang, Y. Li, X. Fan, F. Zhang, and C. Qiu, Acoustic Möbius insulators from projective symmetry, Phys. Rev. Lett. **128**, 116803 (2022).
[12] L. B. Shao, Z. Y. Chen, K. Wang, S. A. Yang, and Y. X. Zhao, Spinless mirror Chern insulator from projective symmetry algebra, Phys. Rev. B **108**, 205126 (2023).
[13] T. Li, L. Liu, Q. Zhang, and C. Qiu, Acoustic realization of projective mirror Chern insulators, Commun. Phys. **6**, 268 (2023).
[14] X. Xiang, F. Gao, Y. Peng, Q. Sun, J. Zhu, and X. Zhu, Acoustic mirror Chern insulator with projective parity-time symmetry, arXiv:2209.02349 (2023).
[15] Y. X. Zhao, C. Chen, X. L. Sheng, and S. A. Yang, Switching spinless and spinful topological phases with projective PT symmetry, Phys. Rev. Lett. **126**, 196402 (2021).
[16] Y. Meng, S. Lin, B. Shi, B. Wei, L. Yang, B. Yan, Z. Zhu, X. Xi, Y. Wang, Y. Ge, S. Yuan, J. Chen, G. Liu, H. Sun, H. Chen, Y. Yang, and Z. Gao, Spinful topological phases in

acoustic crystals with projective PT symmetry, Phys. Rev. Lett. **130**, 026101 (2023).
[17] H. Xue, Z. Y. Chen, Z. Cheng, J. X. Dai, Y. Long, Y. X. Zhao, and B. Zhang, Stiefel-Whitney topological charges in a three-dimensional acoustic nodal-line crystal, Nat. Commun. **14**, 4563 (2023).
[18] X. Xiang, X. Ni, F. Gao, X. Wu, Z. Chen, Y. Peng, and X.-F. Zhu, Demonstration of acoustic high-order Stiefel-Whitney semimetal in bilayer graphene sonic crystals, arXiv:2304.12735 (2023).
[19] C. Zhang, Z. Y. Chen, Z. Zhang, and Y. X. Zhao, General theory of momentum-space nonsymmorphic symmetry, Phys. Rev. Lett. **130**, 256601 (2023).
[20] Z. Y. Chen, S. A. Yang, and Y. X. Zhao, Brillouin Klein bottle from artificial gauge fields, Nat. Commun. **13**, 2215 (2022).
[21] Y.-L. Tao, M. Yan, M. Peng, Q. Wei, Z. Cui, S. A. Yang, G. Chen, and Y. Xu, Higher-order Klein bottle topological insulator in three-dimensional acoustic crystals, arXiv:2305.09174 (2023).
[22] Y. Wang, C. Zhang, Z. Y. Chen, B. Liang, Y. X. Zhao, and J. Cheng, Chess-board acoustic crystals with momentum-space nonsymmorphic symmetries, arXiv:2305.07174 (2023).
[23] Z. Zhu, L. Yang, J. Wu, Y. Meng, X. Xi, B. Yan, J. Chen, J. Lu, X. Huang, W. Deng, C. Shang, P. P. Shum, Y. Yang, H. Chen, G.-G. Liu, Z. Liu, and Z. Gao, Brillouin Klein space and half-turn space in three-dimensional acoustic crystals, arXiv:2305.08450 (2023).
[24] C.-A. Li, J. Sun, S.-B. Zhang, H. Guo, and B. Trauzettel, Klein-bottle quadrupole insulators and Dirac semimetals, Phys. Rev. B **108**, 235412 (2023).
[25] A. G. Fonseca, S. Vaidya, T. Christensen, M. C. Rechtsman, T. L. Hughes, and M. Solijacic, Weyl points on non-orientable manifolds, arXiv:2310.18485 (2023).
[26] Z. Pu, H. He, W. Deng, X. Huang, L. Ye, J. Lu, M. Ke, and Z. Liu, Acoustic Klein bottle insulator, Phys. Rev. B **108**, L220101 (2023).
[27] J. Hu, S. Zhuang, and Y. Yang, Synthetic gauge fields enable high-order topology on Brillouin real projective plane, arXiv:2306.15477 (2023).
[28] Y.-L. Tao, J.-H. Wang, and Y. Xu, Quadrupole insulator without corner states in the energy spectrum, arXiv:2307.00486 (2023).
[29] H. Xue, Y. Yang, and B. Zhang, Topological acoustics, Nat. Rev. Mater. **7**, 974 (2022).
[30] W. Zhu, W. Deng, Y. Liu, J. Lu, H.-X. Wang, Z.-K. Lin, X. Huang, J.-H. Jiang, and Z. Liu, Topological phononic metamaterials, Rep. Prog. Phys. **86**, 106501 (2023).
[31] Y. Yang, J. Lu, M. Yan, X. Huang, W. Deng, and Z. Liu, Hybrid-order topological insulators in a phononic crystal, Phys. Rev. Lett. **126**, 1 (2021).
[32] Y. Qi, C. Qiu, M. Xiao, H. He, M. Ke, and Z. Liu, Acoustic realization of quadrupole topological insulators, Phys. Rev. Lett. **124**, 206601 (2020).
[33] H. Xue, Y. Ge, H.-X. Sun, Q. Wang, D. Jia, Y.-J. Guan, S.-Q. Yuan, Y. Chong, and B. Zhang, Observation of an acoustic octupole topological insulator, Nat. Commun. **11**, 2442 (2020).
[34] X. Ni, M. Li, M. Weiner, A. Alù, and A. B. Khanikaev, Demonstration of a quantized acoustic octupole topological insulator, Nat. Commun. **11**, 2108 (2020).
[35] M. Serra-Garcia, V. Peri, R. Süsstrunk, O. R. Bilal, T. Larsen, L. G. Villanueva, and S. D. Huber, Observation of a phononic quadrupole topological insulator, Nature **555**, 342 (2018).
[36] See Supplemental Material at http://link.aps.org/supplemental/10.1103/PhysRevApplied.21.044002 for (I) designing the PC, (II) calculations of Z_2 invariants (w_x,w_y), (III) calculations of corner charge Q_c, (IV) phase diagrams of the KBI and QI gaps, (V) measured isofrequency contours at other frequencies, and (VI) details of experiments, which includes Refs. [6,7,20,32,38–40].
[37] A. Hatcher, *Algebraic Topology* (Cambridge University Press, Cambridge, 2002).
[38] D. Wang, Y. Deng, J. Ji, M. Oudich, W. A. Benalcazar, G. Ma, and Y. Jing, Realization of a Z-classified chiral-symmetric higher-order topological insulator in a coupling-inverted acoustic crystal, Phys. Rev. Lett. **131**, 157201 (2023).
[39] Z.-G. Chen, L. Wang, G. Zhang, and G. Ma, Chiral symmetry breaking of tight-binding models in coupled acoustic-cavity systems, Phys. Rev. Appl. **14**, 024023 (2020).
[40] Y. Zhou, K. M. Rabe, and D. Vanderbilt, Surface polarization and edge charges, Phys. Rev. B **92**, 041102 (2015).